Atmos. Chem. Phys., 11, 345–361, 2011
www.atmos-chem-phys.net/11/345/2011/
doi:10.5194/acp-11-345-2011

Atmospheric Chemistry and Physics

Mesoscale processes for super heavy rainfall of Typhoon Morakot (2009) over Southern Taiwan

C.-Y. Lin[1], H.-m. Hsu[2], Y.-F. Sheng[1], C.-H. Kuo[3], and Y.-A. Liou[4]

[1]Research Center for Environmental Changes, Academia Sinica, Taipei, Taiwan
[2]National Center for Atmospheric Research, Boulder, Colorado, USA
[3]Department of Geology, Chinese Culture University, Taipei, Taiwan
[4]Center for Space and Remote Sensing Research, National Central University, Jhongli, Taiwan

Received: 20 April 2010 – Published in Atmos. Chem. Phys. Discuss.: 27 May 2010
Revised: 10 December 2010 – Accepted: 29 December 2010 – Published: 14 January 2011

Abstract. Within 100 h, a record-breaking rainfall, 2855 mm, was brought to Taiwan by typhoon Morakot in August 2009 resulting in devastating landslides and casualties. Analyses and simulations show that under favorable large-scale situations, this unprecedented precipitation was caused first by the convergence of the southerly component of the pre-existing strong southwesterly monsoonal flow and the northerly component of the typhoon circulation. Then the westerly component of southwesterly flow pushed the highly moist air (mean specific humidity >16 g/kg between 950 and 700 hPa from NCEP GFS data set) eastward against the Central Mountain Range, and forced it to lift in the preferred area. From the fine-scale numerical simulation, not only did the convergence itself provide the source of the heavy rainfall when it interacted with the topography, but also convective cells existed within the typhoon's main rainband. The convective cells were in the form of small rainbands perpendicular to the main one, and propagated as wave trains downwind. As the main rainband moved northward and reached the southern CMR, convective cells inside the narrow convergence zone to the south and those to the north as wave trains, both rained heavily as they were lifted by the west-facing mountain slopes. Those mesoscale processes were responsible for the unprecedented heavy rainfall total that accompanied this typhoon.

1 Introduction

Over 2885 mm (112.4 inches) rainfall in 100 h, much more than the mean annual precipitation, was recorded at A-Li Shan station (23.5° N and 120.8° E, 2413 m in elevation) as typhoon Morakot (2009) traversed the island of Taiwan over 5 days (6–10 August 2009). It was the heaviest total rainfall for a single typhoon impinging upon the island ever recorded. This typhoon has set many new records in Taiwan. Nine of the ten highest daily rainfall accumulations in the historical record were made by typhoon Morakot, according to the Central Weather Bureau (CWB). Among them, Wei-Liou San station (elevation about 710 m in Southern Taiwan; 22.82° N and 120.66° E) recorded as high as 1403 mm rainfall in one day, 8 August. Table 1 provides a list of the 10 highest rainfall accumulations by typhoons during the last 50 years in which two types of typhoon passages were characterized. One traverses the Central Mountain Range (CMR), the primary island mountain, in the summer (June to August), and the other one passes nearby the island with northeasterly monsoon flow in the fall (September to November). Morakot is the first typhoon simultaneously accompanied with a strong southwesterly monsoon and it generated 2 to 3 times more mean daily rainfall than the nine other strongest typhoons during the last 50 years (Table 1). Typhoon Morakot also was responsible for a vast area, over the western hilly regions of the Central Mountain Range, receiving more than the one year average precipitation (2000 mm) in just 3 days (7–9 August).

This unprecedented rainfall accumulation and area covered are bound to cause disasters. In just three days, there were enormous landslides triggered in mountainous terrain and severe flooding blanketed large areas of lowlands. One particular landslide occurred in the early morning on 9 August, burying the entire village of Xiaolin (elevation around 345 m located at valley, 120.65° E and 23.17° N, in Kaohsing county in Southern Taiwan), killing more than 600 people in this village alone. The area damaged by the landslides, estimated by satellite FORMOSAT-2 (http://www.satimagingcorp.com/satellite-sensors/formosat-2.html), was 241.7 acres. The village of Xiaolin with nearly 394 houses

Correspondence to: C.-Y. Lin
(yao435@rcec.sinica.edu.tw)

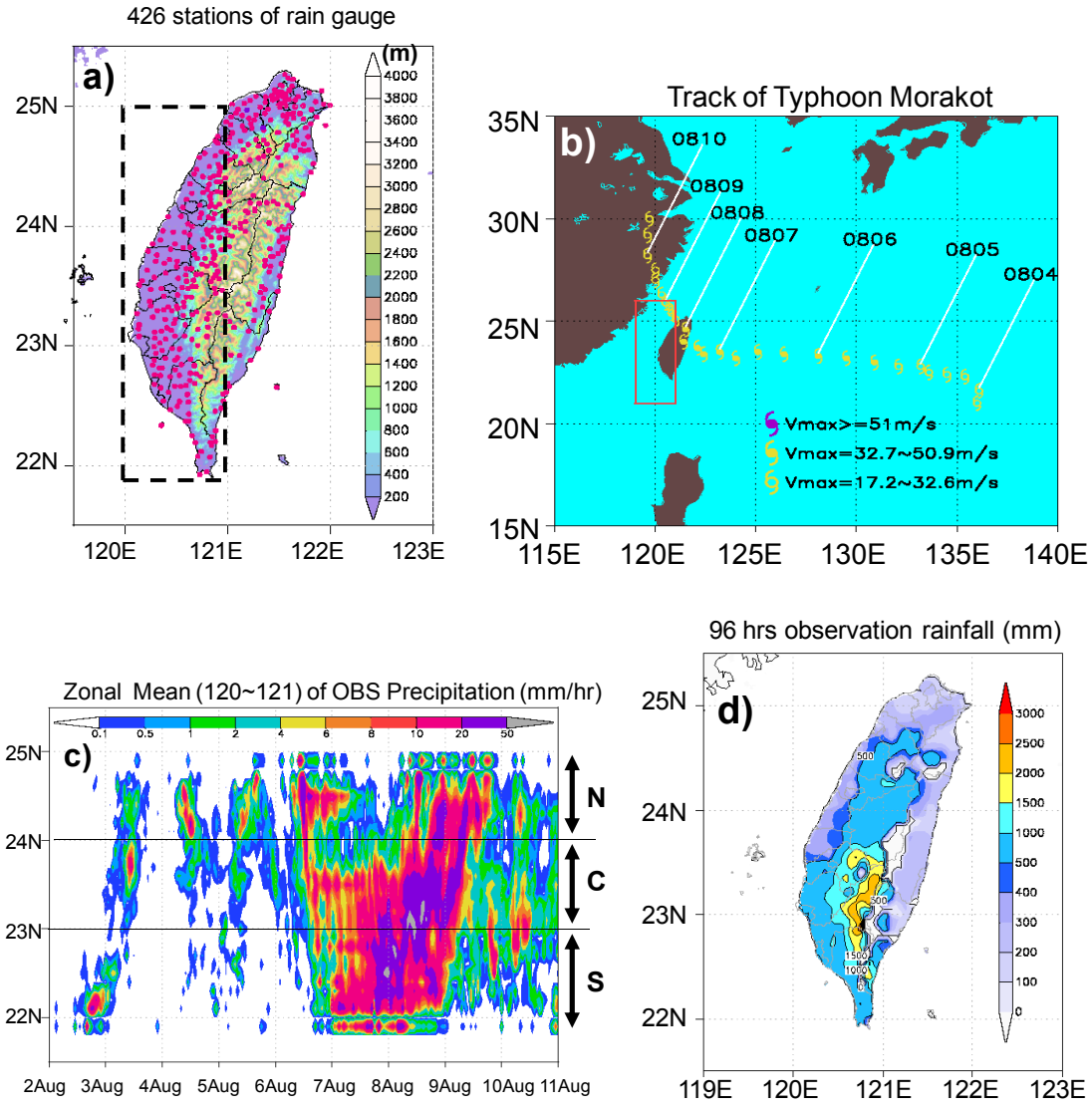

Fig. 1. (a) Spatial distribution of the 426 rain gage stations monitoring network (red dots) and topographic elevation over Taiwan. The black dashed rectangle is the area for which rainfall is displayed in **(c)**. **(b)** The best track for Typhoon Morakot (2009). Colored solid (open) typhoon symbol indicates the best track and the intensity of typhoon at 6-h intervals. **(c)** Spatial and temporal variations of the average rainfall in 0.1 deg latitude increments between 120 and 121° E over western Taiwan **(d)** 96-h rainfall accumulation from 00:00 UTC 06 to 00:00 UTC 10 August 2009.

and the nearby woodland were covered by mud completely. Roughly NT$16.4 billion (∼US$ 0.5 billion) in agricultural damage alone has been estimated over Taiwan because of this tragic event. The official estimate of all the damage and reconstruction costs is beyond NT$ 100 billion (∼US$ 3.03 billion).

As typhoons pass over the island of Taiwan and its vicinity, the local rainfall is strongly affected by the island mountains, particularly the Central Mountain Range (CMR). The CMR occupies about two-thirds of Taiwan's land mass (300 km · 100 km), and is oriented approximately N–S (Fig. 1a) with an average terrain height of about 2000 m (Chen and Li, 1995; Lin and Chen, 2002) and a few steep peaks of almost 4 km. It is well known that damages are strongly related to the location of the typhoon's landfall and interactions between its circulation and the CMR (Brand and Blelloch 1974; Wu and Kurihara, 1996; Wu and Kuo, 1999; Lin et al., 2001; Chien et al., 2008; Ge et al., 2010). Previous studies pointed out that enormous amounts of rainfall occur and are enhanced due to mountain lifting when a typhoon passes over the CMR (Wu and Kuo, 1999; Lin et al., 2001, 2002; Wu et al., 2002; Yang et al., 2008). Moreover, it

Table 1. Record of the 10 highest typhoon rainfall accumulations during the last 50 years. Stations' elevation for A-Li station, An Pu and Chu Tze Hu are 2413 m, 826 m and 607 m, respectively (TC: Tropical Cyclone, NE: Northeasterly, SW: southwesterly).

Typhoon name (CWB warning period)	Intensity classification* Characteristics	Accumulation rainfall in mm (duration) station	Casualties including Death and missing
MORAKOT 5–10 August 2009	Intermediate TC Traversing CMR+ SW monsoon	2855 mm (100 h) A-Li Shan	695
FLOSSIE 1–7 October 1969	Intermediate TC nearby + NE monsoon	2162 mm (120 h) An Pu	105
HERB 29 July–1 August 1996	Strong TC Traversing CMR	1987 mm (48 h) A-Li Shan	73
LYNN 23–27 October 1987	Strong TC nearby + NE monsoon	1497 mm (96 h) Chu Tze Hu	63
SINLAKU 9–17 September 2008	Strong TC Traversing CMR	1458 mm (96 h) A-Li Shan	21
ORA 11–14 October 1978	Intermediate TC nearby + NE monsoon	1434 mm (96 h) Chu Tze Hu	7
GLORIA 8–13 September 1963	Strong TC nearby + NE monsoon	1433 mm (96 h) A-Li Shan	363
NARI 6–20 September 2001	Intermediate TC Traversing CMR	1304 mm (72 h) Chu Tze Hu	104
HAITANG 16–20 July 2005	Strong TC Traversing CMR	1216 mm (72 h) A-Li Shan	15
MINDULLE 28 June–2 July 2004	Intermediate TC Traversing CMR	1182 mm (72 h) A-Li Shan	45

* The CWB's classification of typhoons is based on the maximum wind speed: the light typhoon: 17.2∼32.6 m/s; the intermediate typhoon: 32.7∼50.9 m/s; the severe typhoon: $\geqq$51 m/s

is common that the strong southwesterly flow follows the departure of an invading typhoon and brings heavy rainfall over central or Southern Taiwan (Lee et al., 2008; Chien et al., 2008). Sometimes, such rainfall associated with the southwesterly flow can be significantly heavier than the rainfall brought by the typhoon itself (Chien et al., 2008).

The large-scale setting for the track and intensity of any tropical cyclone are important (Hong et al., 2010), but the primary cause for the extreme rainfall may vary. Ge et al. (2010) suggested the critical role of the CMR and the large-scale conditions for Morakot in their numerical experiments. Here, we apply a numerical model (ARW) to identify the mesoscale processes that might explain what we observed in the data analysis. The processes are, first, that this unprecedented precipitation was caused by the convergence of the southerly component of the pre-existing southwesterly flow and the northerly component of the typhoon circulation. Then, secondly, the westerly component of southwesterly flow from the South China Sea added to the system to push the highly moist air eastward against the CMR, and forced it to lift in the preferred area. The coexistence of both processes was responsible for the unprecedented heavy rainfall. In fact, this combination of processes can be revealed in large-scale meteorological analysis data when analyzed in conjunction with the station data.

2 Data sources and model description

We analyzed the rainfall data from stations (Fig. 1a; red dots, 426 stations in total) in the CWB monitoring network as well as the archived radar and satellite data of CWB. Moisture flux and air flows were deduced from the National Center for Environmental Prediction (NCEP) Global Forecast System (GFS) $0.5^\circ \times 0.5^\circ$ analysis data sets (26 vertical levels) at a 6 h interval.

The Advanced Research WRF (Weather Research and Forecast) model has been configured for the numerical experiments of Morakot. In order to provide detailed and dynamically consistent information of this typhoon, the results of rainfall from one particular simulation are assessed by collocation with CWB rain gauge measurements, further

illustrating the usefulness of numerical models. The details of the Advanced Research WRF (ARW) can be found in Skamarock et al. (2008). The initial and boundary conditions for the ARW simulation are interpolated from NCEP/GFS data sets. In this simulation, the Yonsei-University and the WRF Single-Moment 5-class schemes were selected for the planetary-boundary-layer and microphysics parameterizations, respectively. There were 45 vertical levels and the lowest level was about 50 m above the surface. The horizontal resolution was uniformly 3 km in both directions, with $1081 \cdot 691$ grid-points. Cumulus parameterization may not be necessary at this resolution (Knutson et al, 2007). Thus, no cumulus parameterization was activated in the simulation presented here. To ensure that this event was well simulated, the four-dimensional data assimilation scheme was activated based on the NCEP-GFS analysis data. We have 12 h to spin up the simulation, i.e. we run starting from 12:00 UTC 5 August.

3 Data analysis

3.1 Typhoon track and rainfall

Figure 1b shows the best track of Morakot and indicates that the typhoon began as a tropical depression near 135° E, 20° N on 4 August and continuously moved westward. After upgrading to an intermediate typhoon (category-2 intensity) (Fig. 1b) with maximum wind speed at nearly 40 m/s during 5 August, it approached Taiwan on 6 August. Since Morakot made landfall at 18:00 UTC 7 August, it quickly was downgraded to a light typhoon (maximum wind speed was less than 32.6 m/s). Its structure became asymmetric and a distinctive eye did not seem to exist. Meanwhile, the storm had a very incoherent structure with a broad rainband 150–300 km wide, east of center, with radius of curvature 250 km covering the entire island of Taiwan (Fig. 2a–b). After departing Taiwan on 7 August (Fig. 1b), the typhoon moved slowly.

After averaging the measured rainfall data in the 0.1 latitude interval from 21.8° N and 25.0° N between 120 and 121° E (bounded by the black dashed square in Fig. 1a), the rainfall evolution spanning this square from south to north is displayed between 00:00 UTC 02 and 00:00 UTC 11 August (Fig. 1c). Intermittent rainfall over the western slopes of the CMR lasted for at least 4 days (12:00 UTC 2 August ∼12:00 UTC 6 August) before Morakot's circulation first impinged upon Taiwan. The 24-h rainfall totals in these first 4 days were limited to 150 mm and were supported by moist southwesterly flow in the lower troposphere. In fact, as described in Sect. 3.2, this southwesterly flow had come from the South China Sea since 2 August and continued to prevail since (as shown later in Fig. 3b–d).

The latitudinal extent is divided into three regions from northern to Southern Taiwan, named N, C, and S, which ranges from 24.0 to 25.0° N, from 23.0 to 24.0° N and south of 23.0° N, respectively (Fig. 1c). Only weak intermittent rainfall occurred over mountainous areas during 3–5 August before the typhoon affected Taiwan. Significant, sustained precipitation began over the area near 22° N after 7 August, especially around 00:00 UTC 8 August, and then gradually moved northward through the region C between 22.4° N and 23.6° N, ending about 06:00 UTC 9 August. After it made landfall on the eastern coast of Taiwan (18:00 UTC 7 August), Morakot weakened and lost its eye-wall structure as shown by radar and satellite images (Fig. 2a, b). On the western side of the CMR, the lower-tropospheric wind was dominated by northerlies over the northern half while southerlies dominated the southern half of the island (see Fig. 3). Subsequently, precipitation began to increase significantly over region S from 12:00 UTC 6 August and became torrential on the hilly areas after 12:00 UTC 7 August for about 24 h (Fig. 1c). During this period, more than 1000 mm was pouring down in a narrow N-S belt (about $50 \cdot 25\,\mathrm{km}^2$) over the mountainous areas. As described earlier, a tragic landslide occurred in the early morning of 9 August and buried the entire village of Xiaolin. Morakot made landfall again after 12:00 UTC 9 August on the southeast coast of China. However, following Morakot's departure from Taiwan, as much as 350 mm additional rainfall accumulation took place during the following 24 h (i.e. on 10 August) (Fig. 1c) over the already seriously damaged areas of Southern Taiwan. This additional rainfall was generated by the following southwesterly flow with its high moisture content at 900 hPa with specific humidity >15 g/kg and wind speed as high as 20 m/s, i.e. moisture flux >300 g/kg m/s at 900 hPa (Fig. 3c).

Also shown in Fig. 3, over the Southern Taiwan Strait and southwestern Taiwan, the northerly flow as a part of the typhoon evolved to the westerly, and then southwesterly, flow as the typhoon slowly moved northward in these 3 days. The movement and strengthening of the southwesterly flow into this region is not uncommon when a typhoon departs from Taiwan, and the accompanying moisture provides the source for heavy rainfall as the southwesterly flow impinging the local topography (Chien et al., 2008; Lee et al., 2008).

3.2 Sources of water vapor

Horizontal moisture fluxes in the lower troposphere were computed using the NCEP/GFS analysis data, they were then vertically averaged below 700 hPa (about 3 km) and zonally averaged between 119 and 121° E (the red square in Fig. 1b). Figure 4 shows the evolution of the zonal mean for vector water vapor flux ($q \times U\hat{i} + q \times V\hat{j}$, where q = specific humidity), the zonal flux component ($q \times U$), and meridional component ($q \times V$) from 2 to 11 August over a latitudinal extent between 21 and 26° N. The contour lines denote wind speeds, while color shades represent the magnitude of the water vapor fluxes.

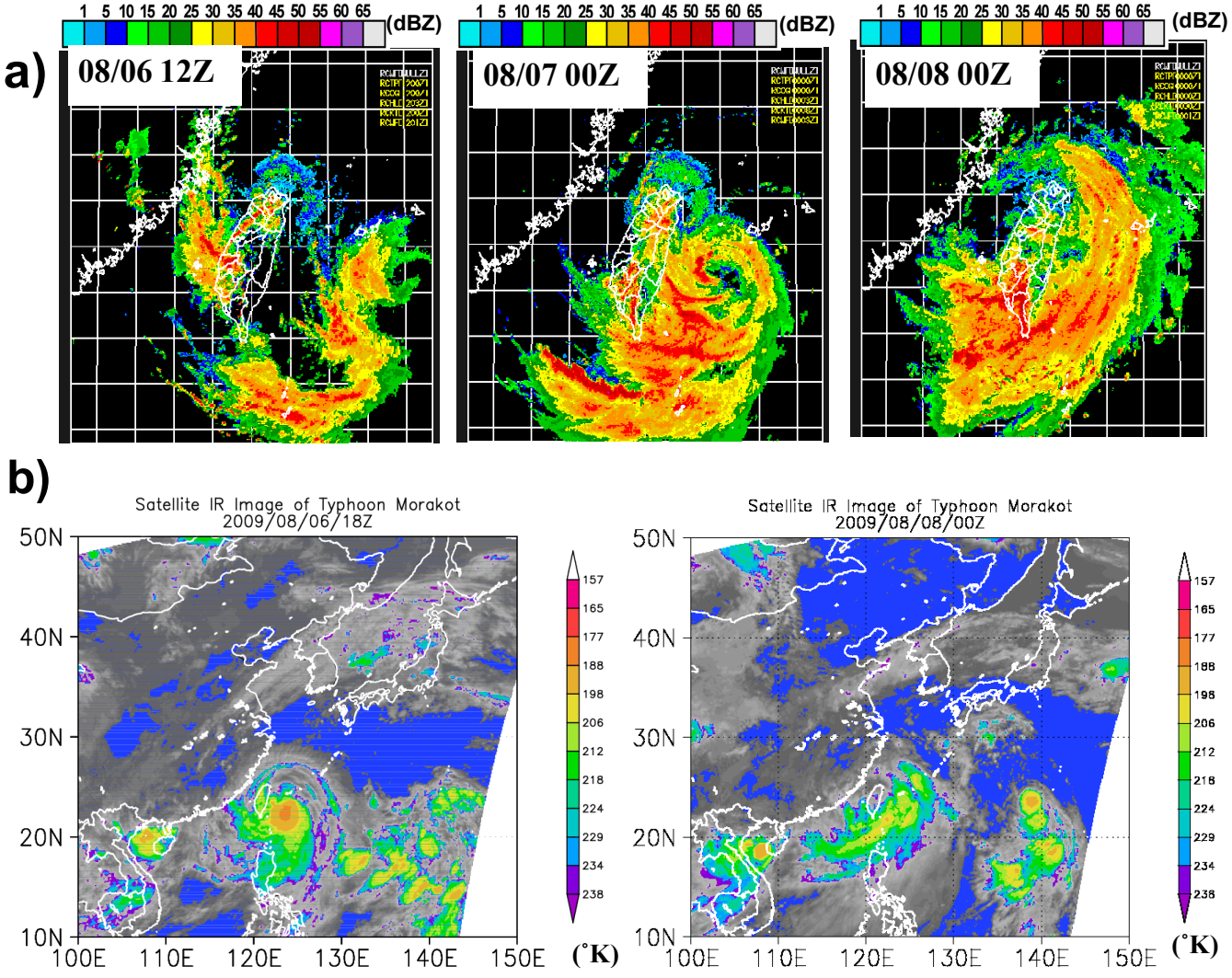

Fig. 2. (a) Composite of the maximum radar reflectivity in a volume (colored) at 12:00 UTC 6, 00:00 UTC 7 and 00:00 UTC 8 August, 2009. **(b)** Infrared Satellite image from Japan MTSAT satellite at 18:00 UTC 06 and 00:00 UTC 8 August 2009. The colored areas represent cold brightness temperatures (°K).

The moisture flux shown in Figs. 3a–b and 4a displays a classical pattern of a tropical cyclone traversing the island. The moisture transport was mostly southerly before the arrival of Morakot. The passing of Morakot brought in a large amount of moisture in a cyclonic pattern around 7 August, mostly in Southern Taiwan. After Morakot left the region (the red square in Fig. 1a) during 10 August, the moisture flux decreased to an overall southwesterly pattern.

Furthermore, for the E-W component (Fig. 4b), along 22.5° N (and farther south), the moisture flux >200 g/kg m/s (colored) started from 12:00 UTC 6 August and significantly increased to >500 g/kg m/s from 12:00 UTC 7 August to 12:00 UTC 8 August. The enormous moisture flux, > 500 g/kg m/s, with strong westerly wind, >20 m/s (solid line in Fig. 4b), moved from the ocean toward inland including the mountainous areas and extended northeastward to 23° N around 00:00 UTC 8 August (Fig. 4b). This is consistent with the torrential rains recorded in region S at the same time (Fig. 1c) and also agrees with the spatial distribution of extreme rainfall accumulation from the coastal plain area to CMR (Fig. 1d). In the evolution of the N-S component of the moisture flux from 2 August to 11 August (Fig. 4c), the southerly high moisture flux (>200 g/kg m/s) with wind speed >10 m/s already existed prior to 3 August before Morakot approached Taiwan. In other words, the southwesterlies with high moisture content prevailed during early August and lasted to 11 August at least in the lower troposphere (Fig. 4b and c). The strong southerly component of

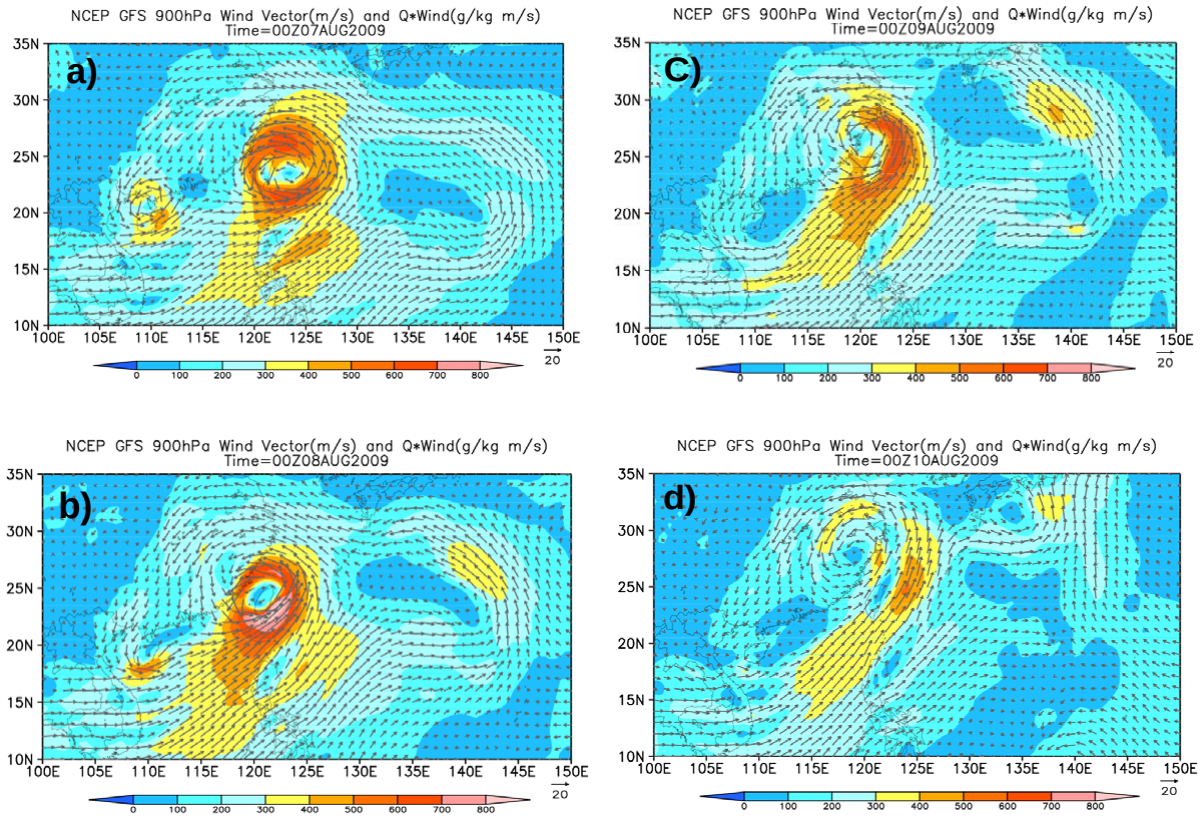

Fig. 3. (a) Moisture flux (colored) and wind field (arrow) deduced from NCEP GFS data at 900 hPa level at 00:00 UTC 7 August 2009. The colored scales represent the magnitude of moisture flux. The lower right corner of arrow denotes the scale of wind speed. **(b)** Same as **(a)** but for 00:00 UTC 8 August 2009. **(c)** Same as **(a)** but for 00:00 UTC 9 August 2009. **(d)** Same as **(a)** but for 00:00 UTC 10 August, 2009.

the moisture flux provided the source for the rainfall throughout this period, except for the invasion of the northerly flow of Morakot for a period between 6 August and 8 August. The northerly moisture flux with a wind speed >20 m/s (dashed line) associated with the typhoon invasion enhanced the north-south convergence (Fig. 4c). Consequently the moist southerly flux advanced northward, strengthened and collided with the northerly flux to form a local moisture convergence between 22 and 23° N during 7 August. At this time the N-S convergence was stronger than its E-W counterpart in both the analyzed and simulated results (Fig. 5), and is discussed further in Section 3.4. This essential convergence of these two opposite (N-S) fluxes hence played a key role in the dramatic increase of the rainfall (Fig. 1c) over Southern Taiwan between 00:00 UTC 7 August and 00:00 UTC 8 August. The crucial processes of the heavy rainfall occurrence over southwestern Taiwan are as follows: 1. In the early stages the convergence between the typhoon's flow from the north and the SW monsoon yielded heavy rain 2. Later, the rain was produced more from the zonal convergence and mountain lifting along the CMR.

As Morakot slowly departed from the island and the associated northerly flux shifted northward, both the E-W convergence zone and the westerly moisture flux gradually traversed northward together. Eventually, the northerly flux was completely replaced by a southerly flux over the entire island of Taiwan after 00:00 UTC 9 August (Fig. 4a). However, some precipitation continued as a southerly moisture flux still prevailed. This fits the commonly recognized understanding that a southwesterly flow follows the departure of tropical cyclones from Taiwan.

It is well known that the southwesterly moist flow can contribute to localize rainfall, but cannot alone support extreme amounts. The northerly flow of Morakot's circulation collided with the southerly component of the southwesterly monsoon and produced a low-level convergence. This convergence became a critical factor in the occurrence of significant rainfall over Southern Taiwan during the early stage of heavy rainfall, which is illustrated in the following.

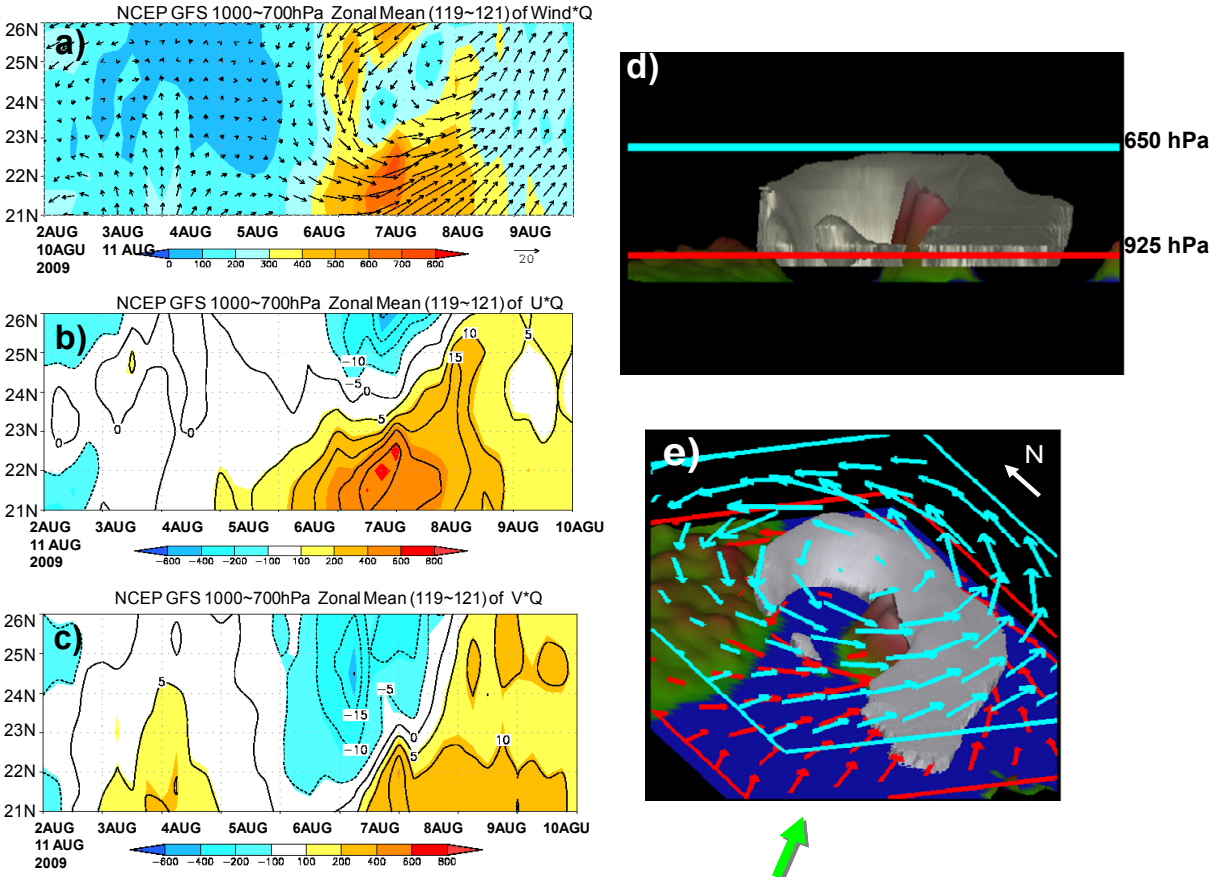

Fig. 4. (a) Temporal variation of average moisture flux (colored) and wind field (arrow) for the zonal mean (119–121° E) and depth between 1000 and 700 hPa deduced from NCEP GFS data. The colored scales represent the magnitude of moisture flux. The lower right corner of arrow denotes the scale of wind speed. **(b)** Temporal variation of the average moisture flux (colored) and wind speed (contour) between 1000 and 700 hPa for the zonal mean (119–121° E) in E-W direction deduced from NCEP GFS data. The colored scales represent the magnitude of moisture flux. **(c)** Same as **(b)** but for in N-S direction. **(d)** A northwest-southeast vertical perspective views for depth by VIS5D for the moisture flux at 00:00 UTC 8 August taken from the direction of the arrow in **(e)** The grey shading is the moisture flux surface of 550 g/kg m/s. **(e)** Three-dimensional perspective views by VIS5D for the moisture flux at 00:00 UTC 8 August. The blue (red) arrow represents the wind field at 650 hPa (925 hPa). The grey shading is the moisture flux surface of 550 g/kg m/s.

3.3 Depth of moisture flux

Figure 4d and e show three-dimensional views in different perspectives for the moisture flux from the southwest (green arrow) at 00:00 UTC 8 August deduced from NCEP data by using VIS5D software (http://www.ssec.wisc.edu/~billh/vis5d.html). Comparing with the Morakot moisture-flux layer farther northeast, the moisture layer from the southwest is really shallow, as seen in the northwest-southeast vertical perspective view (Fig. 4d). The more horizontal view (Fig. 4e) illustrates further that the southwesterly moisture flux was limited to a much lower altitude, below 900 hPa from the ocean surface at the southern end. This view demonstrates that the southwesterly flow is able to provide abundant moisture even though shallow, below 900 hPa at the southern end.

Moreover, Fig. 4e illustrates that the moisture flux gradually thickened toward Morakot's layer in the north. The red and light-blue arrows denote the southwesterly and westerly flows at 925 hPa and 650 hPa, respectively. It is apparent that the process of convergence started at the lower left corner of Fig. 4e and the lower altitude southwesterly flow did not reach the 900 hPa-level as it went into the moisture band. It also shows that the lower altitude southwesterly flow merged into the typhoon circulation and extended much deeper than this level in the north. The co-existence of the tropical southwesterly moist flow in the low atmosphere and the relatively higher Morakot circulation is the key reason for the heavy rain production and wide-spread floods over Southern Taiwan.

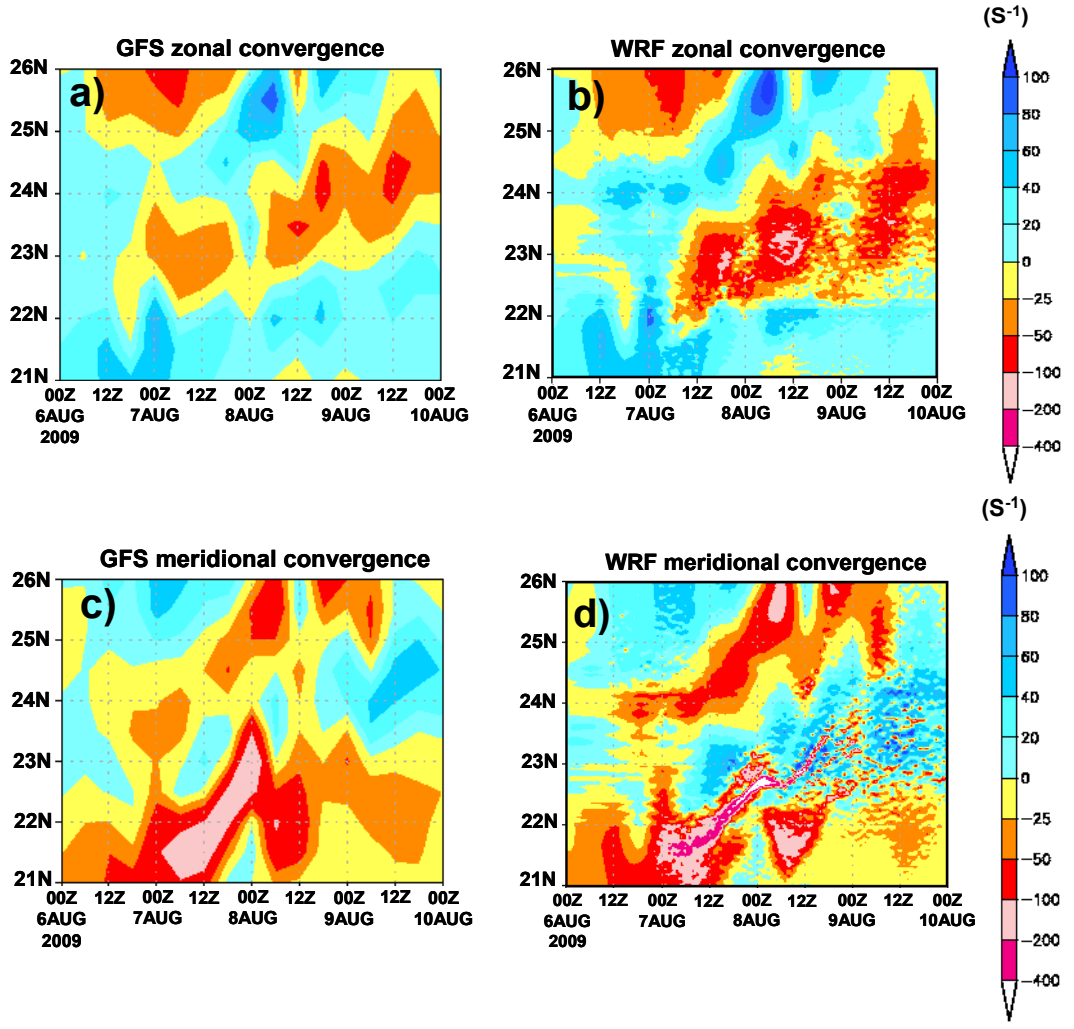

Fig. 5. (a) Temporal variation of wind convergence (negative) and divergence (positive) in E-W direction (colored) between 950 and 700 hPa for the zonal mean (119–121° E) deduced from NCEP GFS data sets. **(b)** Simulated results of the temporal variation of wind convergence (negative) and divergence (positive) in E-W direction (colored) between 950 and 700 hPa for the zonal mean (119–121° E) from WRF model. **(c)** Same as **(a)** but for N-S direction (colored) **(d)** Same as **(b)** but for N-S direction (colored).

3.4 Horizontal convergence

To better understand the evolution of the convergence itself, we averaged the E-W and N-S components of the horizontal convergence derived from the NCEP/GFS analysis between 120 and 121° E, which included the most western plain and hilly regions of Taiwan. These components were then averaged vertically between 950 and 700 hPa to represent the lower-tropospheric convergence. The N-S convergence (Fig. 5c) supported the heavy rainfall (Fig. 1c) during 7 August and early 8 August for the region south of 23° N. As heavy rainfall slowly moved northward after early 8 August, the E-W convergence took over. This shift diminished neither the intensity nor total rainfall, despite the E-W convergence (Fig. 5a) being weaker than its N-S counterpart. While the E-W convergence strengthened, its N-S counterpart became divergent. The two convergence components evidently represent different processes. Figure 4d shows the gradual increase of moisture flux inland. This E-W convergence in the region 23∼24° N continued to support heavy rainfall for at least 3 days along the western hills and slopes of CMR (Fig. 1c). The NCEP/GFS analysis data have a horizontal resolution of about 50 km, which is too coarse to closely represent the convergence intensity. Results from a numerical experiment with higher resolution using ARW are presented next.

4 Model simulation and discussion

The numerical simulation was conducted with a version of the Weather Research and Forecast (WRF) model, the Advanced Research WRF (ARW3.1), for 4 days between 00:00 UTC 06 and 00:00 UTC 10 August. The simulation of 96-h accumulated rainfall (Fig. 6) matched the observations (Fig. 1d) quite well in terms of the rainfall amount and spatial distribution. We further plotted the time series of the E-W and N-S components of averaged convergence (Figs. 5b, d) as done with NCEP/GFS data (Fig. 5a, c). Overall, the evolution from the simulation is comparable to those from the analysis. One striking difference in the N-S components of the mean convergence is that the peak model values (Fig. 5d) are locally much stronger than those of the analysis (Fig. 5c), because of the difference in resolution. This convergence was the primary reason for the heavy rain in the S region (south of 23° N), as seen in Fig. 1c. Moreover, the E-W component of the convergence from the ARW simulation (Fig. 5b) was much stronger than that from the NCEP/GFS analysis (Fig. 5a), particularly for the latitudinal band between 23° N and 24° N. The dramatic enhancement of local maximum values obtained at 3 km resolution (Fig. 5b), relative to those of the coarser analysis data, is obvious. This enhancement of the convergence from model results indicates the significance of topographic lifting for producing the heavy rain during 8–9 August when the N-S convergence was relatively weakened.

Figure 7 contains vertical velocity fields (positive in red and negative in blue) and potential vorticity contours (positive in black and negative in green) in the dashed rectangle of Fig. 8a at 6 h interval from 06:00 UTC 7 August to 00:00 UTC 8 August. Two distinct larger-scale bands of vertical motions were the prominent features in Fig. 7, and their associated rainbands can be identified in the composite radar reflectivity (Fig. 2a). The land-locked band on the western side of the CMR was topographically related, and it is not directly related to the typhoon circulation. The other band was oriented in a northwest-southeast direction over the Southern Taiwan Strait and moved from a more north-south orientation to a more east-west one under a gradually strengthening southerly component of the southwest monsoon (Fig. 5). Thus, the southern end of this band eventually made landfall to interact with the southern part of the CMR where the heavy rainfall occurred. This larger-scale band is thus termed the main rainband in this paper. Within the main rainband over the Taiwan Strait, the wavy patterns in vertical velocity (W) and potential vorticity anomaly (PV) were clear at all four recording times lasting a total of 18 h. The positive W's mostly collocated with the positive PV's. Sometimes, the negative PV's appeared in a couplet form with the positive PV's, but associations of the negative PV's with the negative W's were hardly observed. The collocations of the positive PV's and the positive W's suggest the presence of "vortical hot towers" (VHT's; Hendricks et al., 2004; Montgomery et al., 2006). Such co-locations frequently appeared in both horizontal and vertical cross sections in our fine-resolution numerical simulations. As suggested by Hendricks et al. (2004) and Montgomery et al. (2006) that VHT's were the building blocks of tropical cyclones, VHT's were evidently numerous in our simulated main rainband shown in Fig. 7. More interestingly, they were not randomly distributed but organized in the form of wave trains within the main rainband of 200∼400 km long and 50∼100 km wide.

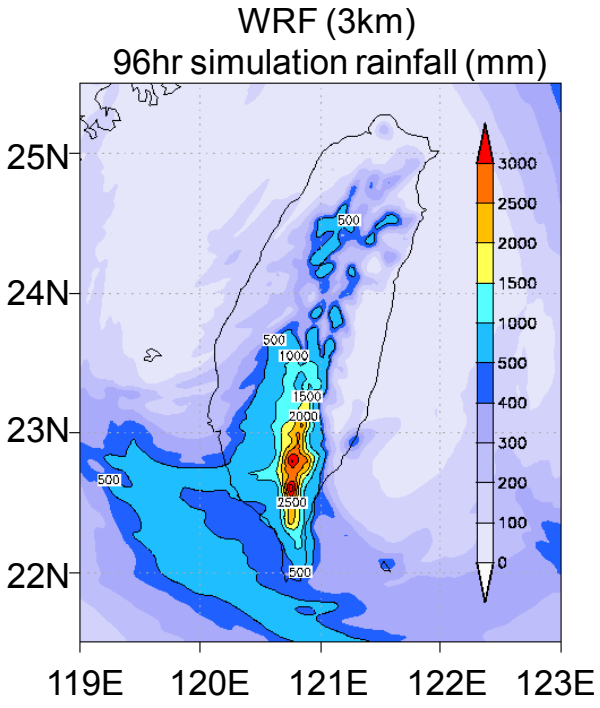

Fig. 6. The simulation accumulated rainfall during 00:00 UTC 06 to 00:00 UTC 10 August 2009 by WRF model.

Also shown in Fig. 7, two types of wave trains propagating differently were separated by the convergence zone. The first wave trains, northeast/north of the zone, propagated along the vortex tangential flow, while the second wave trains southwest/south of the zone propagated away from the vortex. There were long blue filaments of downward motion extended from northwest to southeast. These filaments and the accompanying wave trains on both sides gave the shape of "arrows", which lay at the center of activity when the main rainband slammed into the CMR. The low-level convergence zone supported the upward motion (in red color) on the southern boundary of the main rainband, and the compensating downward motion appeared south of the upward motion (in blue color). The wave trains propagating away from the main rainband may be viewed as the internal gravity waves radiating out of a thermal source. Previous observations (Pfister al., 1993; Sato, 1993; Chane-Ming et al., 2002, 2010; Dhaka et al., 2003, Chun et al., 2007; Ibrahim

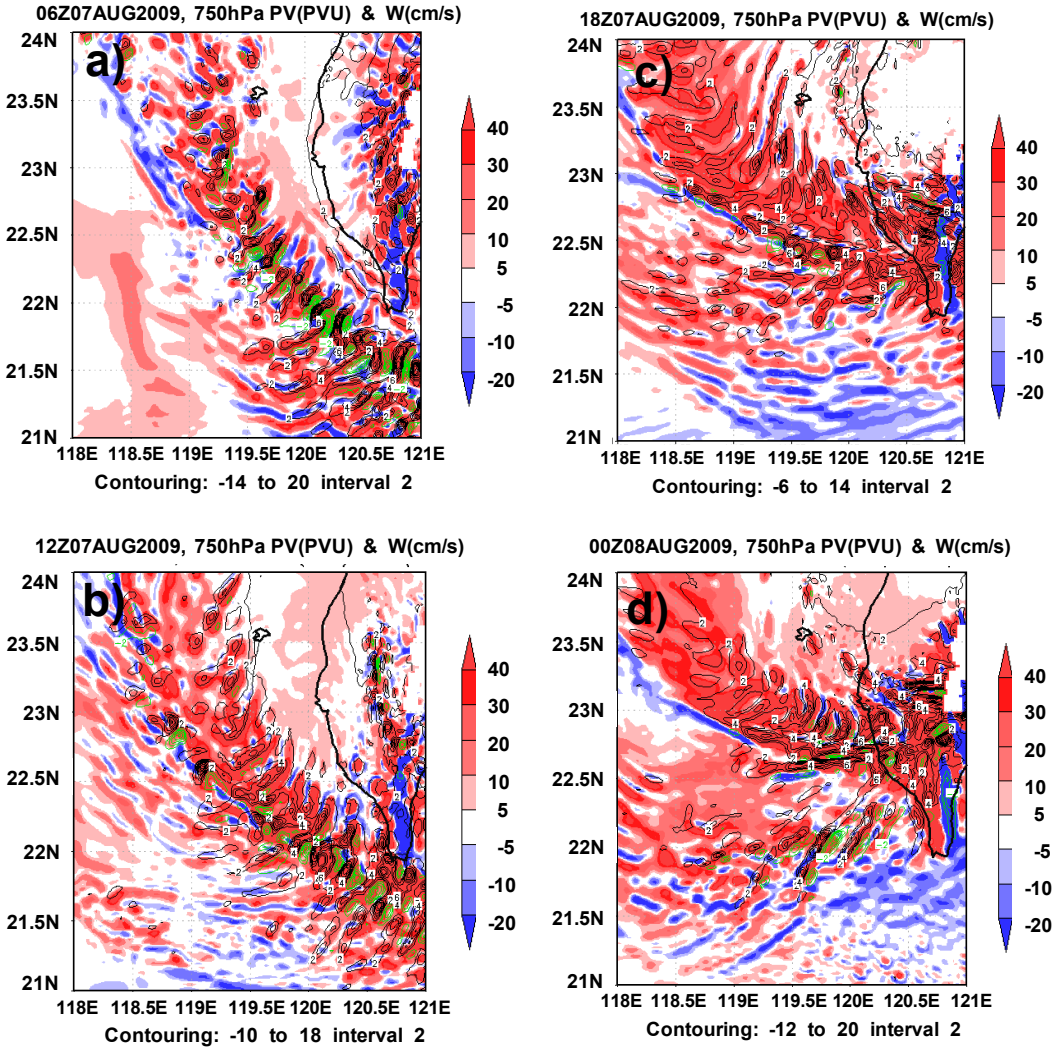

Fig. 7. Simulation of vertical velocity fields (colored shades: positive in red and negative in blue) and potential vorticity (contours: positive in black and negative in green, interval: 2 PVU) at 750 hPa for **(a)** 06:00 UTC 7 August **(b)**, 12:00 UTC 7 August **(c)** 18:00 UTC 7 August and **(d)** 00:00 UTC 8 August.

et al., 2010) and numerical experiments (Kim et al., 2003; Kuester et al., 2008) supported the idea that internal gravity waves can be radiated away from tropical cyclones. This radiation is related to a tropical cyclone's strong sources of latent heat release.

Within these 18 h of typhoon Morakot's evolution, the model results indicate that the main rainband over the Southern Taiwan Strait moved northward under the combined influence of the northward movement of the typhoon itself and the northward advance of the southwest monsoon. Before the main rainband started to interact with the southern part of the CMR, it exhibited a wavy pattern consisting of smaller rainbands in an almost northeast-southwest orientation, which was perpendicular to that of the main rainband. Such smaller rainbands were still present after the eastern end of the main rainband made landfall. Some details of these rainbands are discussed in the following.

Figure 8a shows the surface pressure and vertical velocity fields at 750 hPa, and the typhoon with its surface pressure minimum east of the island of Taiwan at 09:00 UTC 7 August in the simulation. The semi-circular band of W was represented by the clusters of W west and south of the island. Based on the surface circular isobars and W, the typhoon looked to have a disintegrated vortex eyewall of which half was missing, because the typhoon's center region (without much W) was almost as large as the island itself in the simulation. The exception is that there were still some positive W's over the Island. How the typhoon evolved into this

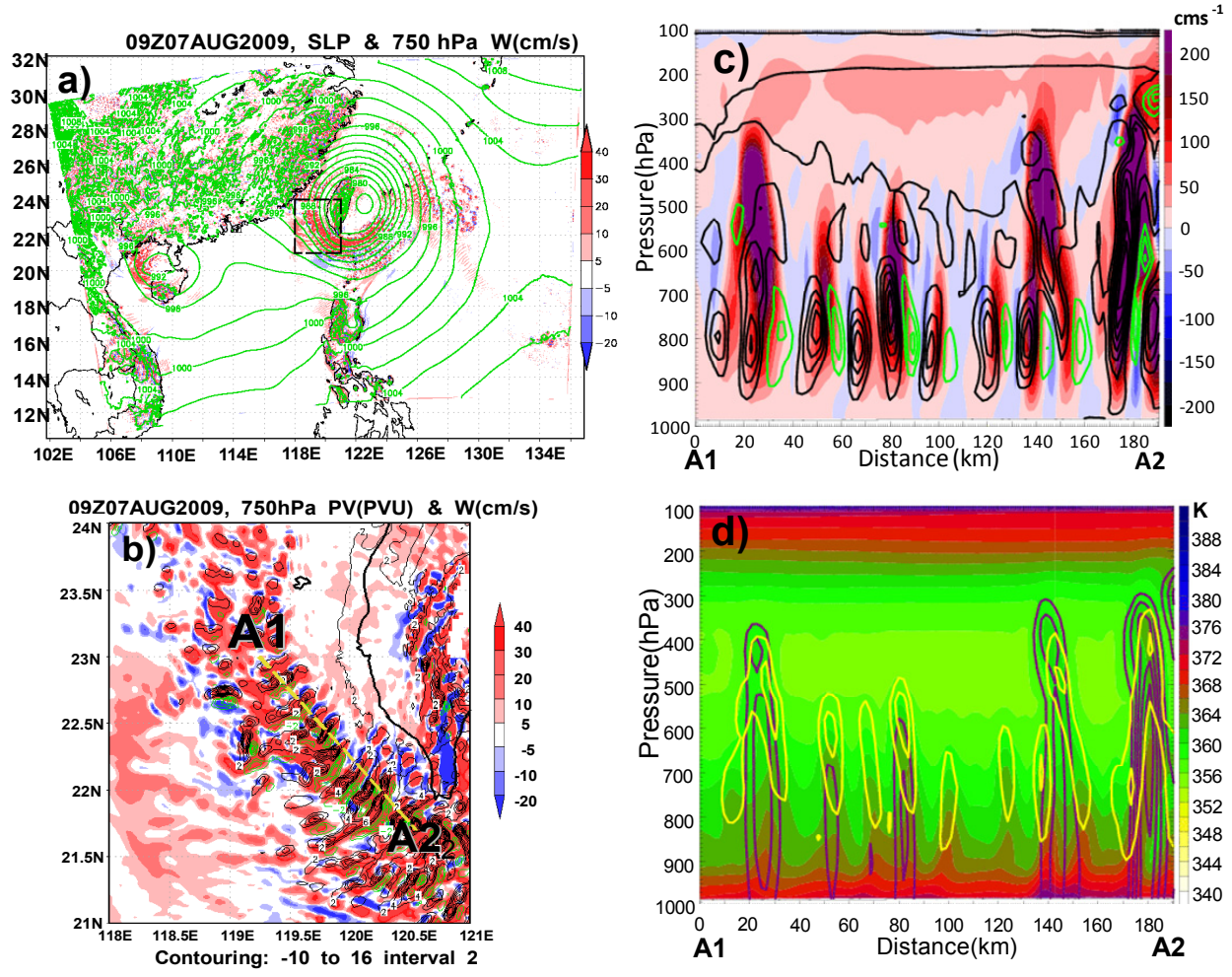

Fig. 8. (a) Simulation of horizontal distribution of surface pressure (contour) and vertical velocity (shaded) at 750 hPa at 09:00 UTC 7 August 2009. **(b)** Same as Fig. 7 but for 09:00 UTC 7 August **(c)** The cross-section distribution along A1–A2 in **(b)** for vertical velocity (shaded) and potential vorticity (Positive in black and negative in green, interval 2 PVU) **(d)** Same as **(c)** but for equivalent potential temperature (shaded), Total precipitation mixing ratio (contour in purple) and total cloud mixing ratio (contour in yellow).

stage is quite interesting and an important question, but it is beyond the scope of this paper. In Fig. 8b, the vertical velocity and potential vorticity fields at 750 hPa over a portion of the region (the black dashed rectangle in Fig. 8a) depict the smaller rainbands within the main one. The orientation of the smaller bands was generally perpendicular to that of the main one. The smaller bands had a wavelength of 20∼30 km and propagated along the orientation of the main band. Such wavy patterns also appeared in the spiral rainbands described in a recent publication (Qiu et al., 2010, their Fig. 6). In their case, the vortex eye of the simulated tropical cyclone was occupied by a full core of PV, and PV perturbations were episodically stripped off from the vortex edge to become part of the outer spiral rainband. However, in our case, there was no vortex PV core during this period, but our PV perturbations were in a wave-train form within the main rainband.

A vertical cross-section A1-A2 (from 23° N, 119.25° E to 21.7° N, 120.55° E) along the orientation of the main band is presented in Fig. 8c and d for the vertical velocity (W), potential vorticity (PV), equivalent potential temperature (θ_E), and mixing ratios of cloud condensates (Q_{cl}, cloud droplets and ice) and precipitation condensates (Q_{pr}, raindrops and snow) from 1000 to 100 hPa. The W and PV fields (Fig. 8c) indicate the wavy characteristics as well as the PV couplet features associated with upward motions. The association of the positive W and the positive PV for the tropical cyclone growth and axisymmetrization process has been reported recently (Hendricks et al., 2004; Montgomery et al., 2006). However, the co-existence of the positive and negative PV's in the couplet form within positive W's in the lower half of the troposphere may shed further insight into the growth of convective cells. Franklin et al. (2006) showed that the

vorticity coupling was the consequence of the tilting of the low-level horizontal vortex tubes by an updraft (Weisman and Davis, 1998). Such PV couplets also appeared in the fine-resolution numerical simulation of Qiu et al. (2010). As shown in Fig. 8c, the PV couplet had only one negative and one positive PV within one updraft most of the time. The PV couplet, updraft, and convective cloud/rain cell were all co-located in a wave-train form. Some of the larger cells extended to the upper troposphere, but the smaller ones remained in the lower troposphere. The roles of both larger and smaller cells in this complex cell-growing process require further investigation. We will report dynamical/physical contributions of those convective cells to heavy rainfall in the near future.

It is well known that one of the primary energy sources for the development of tropical cyclones is the latent heat flux from the warm ocean surface. Equivalent potential temperature (θ_E), and mixing ratios of cloud condensates (Q_{cl}), and precipitation condensates (Q_{pr}) along the cross-section mentioned above are presented in the Fig. 8d. The updrafts and cloud/rain cells, (represented by the contours Q_{cl} and Q_{pr}) were directly related and co-located. Moreover, the surges of high θ_E from the ocean surface to support the convective cells are obvious in Fig. 8d. The co-locations of these θ_E surges to the positive PV cells provide evidence for the diabatic generation of localized PV appearing in Fig. 8c. Such co-locations can be found generally in the main rainband studied here, as it traversed over the ocean surface.

Also, along this cross-section, the variables W, PV, θ_E and Q sum (the sum of Q_{cl} and Q_{pr}) were extracted at 750 hPa from 06:00 UTC to 12:00 UTC 7 August, and their time evolutions are shown as Hovmoller diagrams in Fig. 9a and b. An almost constant propagation of the smaller rainbands with an apparent downstream speed of about 20 m/s was a common feature in the W and PV fields (Fig. 9a) and the θ_E and Q sum fields (Fig. 9b), while the typhoon flow speed at this altitude was about 30 m/s during these times. Obviously, these convective rainbands were not completely steered by the tangential flow of the typhoon. Furthermore, there was a strong suspicion of a much slower upstream propagation with a speed of less than 2 m/s. The signature of this upstream propagation is much less uniform and weaker than that of the downstream one.

To understand the convergence zone found in the half-degree-resolution analysis data and our 3-km-resolution numerical results from ARW, some analyses are presented for 17:00 UTC 7 August when the typhoon moved slowly northward and the southwest monsoon also made its northward advance more aggressively. Referring to Fig. 5, convergence began to appear at the southern end of Taiwan near this time. Figure 10a shows the surface pressure field and W field at 750 hPa in the same region as that at an earlier time (Fig. 8a). Compared to the earlier time (Figs. 8b and 10b), the typhoon strengthened during a period of 11 h as indicated by the stronger radial pressure gradient, smaller diameter of

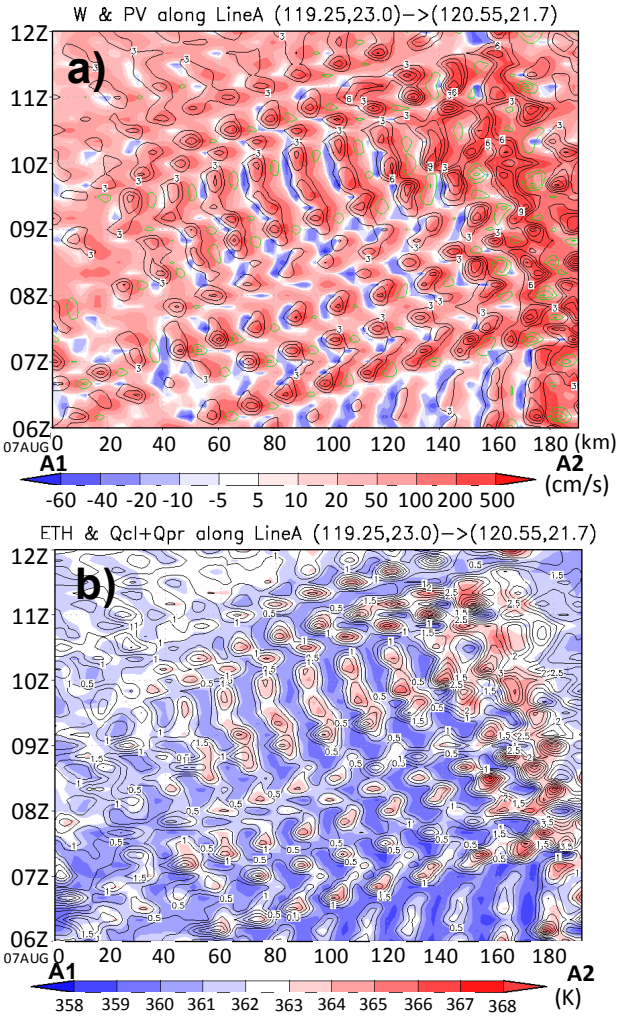

Fig. 9. Simulated results of the temporal variation of along cross-section A1–A2 in **(b)** from 06:00 UTC to 12:00 UTC 7 August. **(a)** Vertical velocity fields (colored shades: positive in red and negative in blue) and potential vorticity (contours: positive in black and negative in green, interval: 2 PVU) **(b)** Same as **(a)** but for theata-e and total precipitation mixing ratio.

the semi-circular band of W (although it still had a diameter of more than 300 km), and more convective cells on the eastern and northern side of the typhoon where convective cells were absent earlier. The semi-circle had grown with the Island in its center. This can be seen as a slow axisymmetrization process. The telescoped region (Fig. 10b) shows the smaller bands inside the main band in the same fashion shown earlier (Fig. 8b), but a convergence zone appeared on the southern boundary of the main rainband as outlined by the cross-section location E1–E2 (from 23° N, 118° E to 22° N, 121° E). The analyses of the same variables along this cross-section are presented as follows.

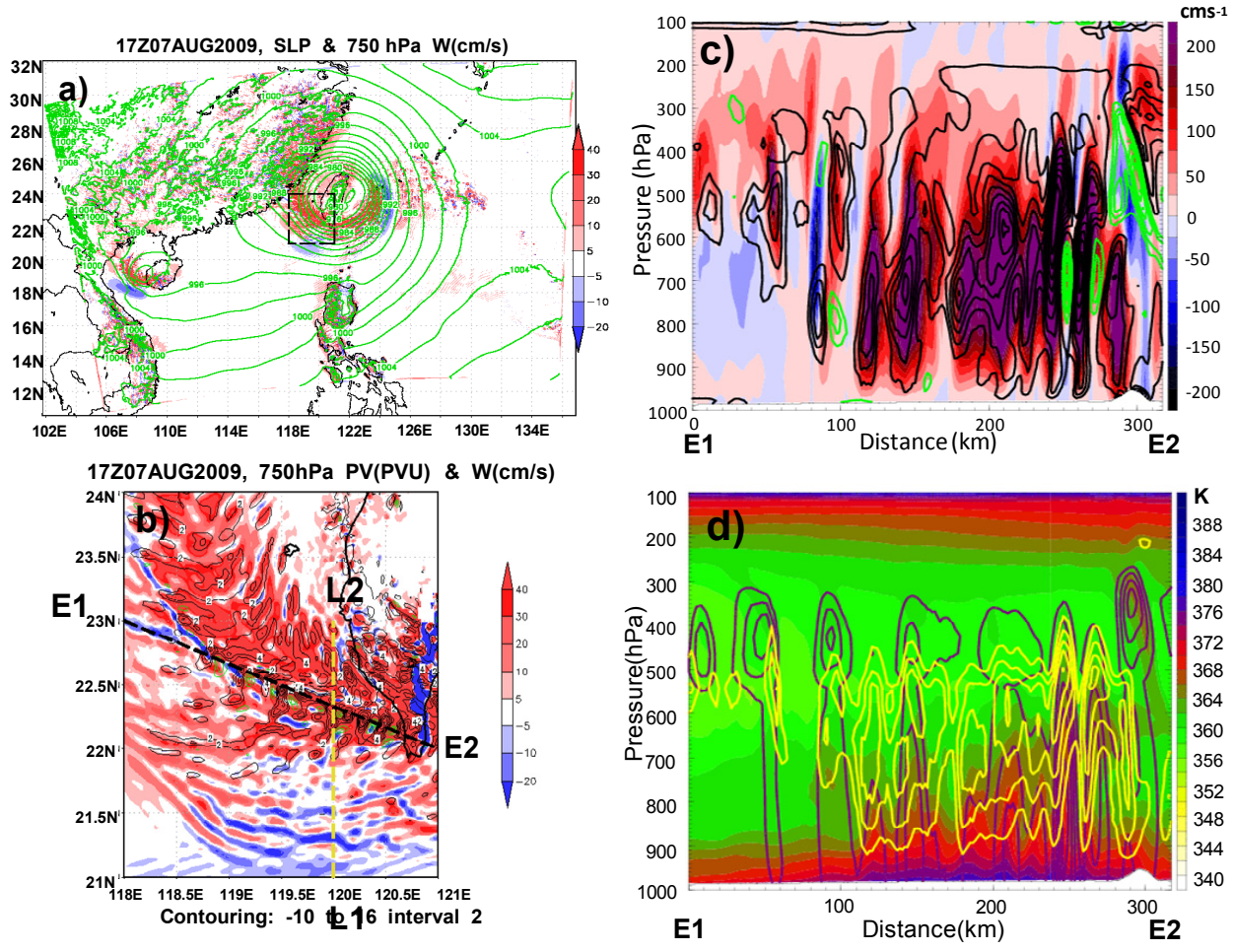

Fig. 10. **(a)** Simulation of horizontal distribution of surface pressure (contour) and vertical velocity (shaded) at 750 hPa at 17:00 UTC 7 August 2009. **(b)** Same as Fig. 8b but for 17:00 UTC 7 August **(c)** The cross-section distribution along E1–E2 in **(b)** for vertical velocity (shaded) and potential velocity (positive in black and negative in green, interval 2 PVU) **(d)** Same as **(c)** but for equivalent potential temperature (shaded), Total precipitation mixing ratio (contour in pink) and total cloud mixing ratio (contour in yellow).

As in the previous cross-section (Fig. 8c), vertical motions and potential vorticity between 1000 and 100 hPa in cross-section E1–E2 are shown in Fig. 10c. On the eastern two-thirds of this cross-section from west-northwest to east-southeast (E1 to E2), the maxima of upward motions and positive PVs could reach 5 m/s and 10 PVU, respectively. Lack of downward motion, both convection and rotation were vigorous. On the other hand, the vertical motions were not only quite minimal but also mostly downward on the western third of the cross-section. Similarly, the equivalent potential temperature had a quite calm structure with much less active convective cells on the western side (Fig. 10d). By contrast, on the eastern two-thirds side, there was a highly perturbed θ_E field right above the ocean surface to support severe convection shown in the cloud (Q_{cl}) and rain (Q_{pr}) fields (Fig. 10d). In fact, the eastern two-thirds of this cross-section was in the convergence zone produced by the typhoon's southward flow from the north and the northward monsoonal flow from the south in the lower atmosphere. Not only convective but also rotational motions were evidently large in the convergence zone. As will be seen soon in a north-south oriented cross-section L1–L2 (Fig. 12), this zone was quite narrow.

Along the cross-section E1–E2, the time evolutions of all the convective cells and the convergence zone at 750 hPa for 6 h (between 14:00 UTC and 20:00 UTC, 7 August) are illustrated in Fig. 11. It was this period during which the Southern Taiwan experienced the initial heavy rainfall (Fig. 1c) and the initial invasion of the typhoon-related rainbands and the associated convergence zone (Fig. 5). Here, both Figs. 11a and b clearly depict the wave-train propagations of convective cells. They had similar wavelengths (20∼30 km) and similar propagation speeds (about 20 m/s), as those in the previous cross-section. At the beginning of the last 5 h, the

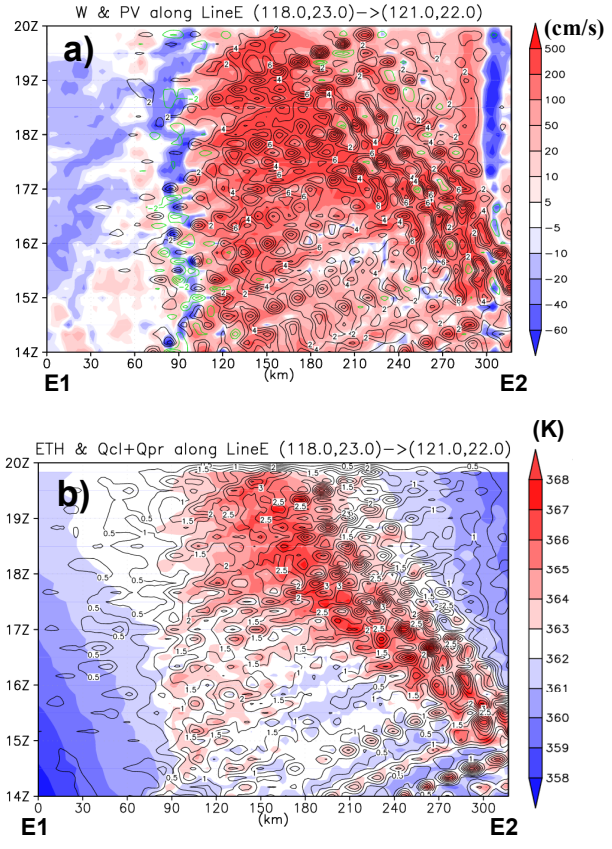

Fig. 11. Simulated results of the temporal variation along cross-section line E1–E2 in Fig. 10b from 14:00 UTC to 20:00 UTC 7 August. **(a)** vertical velocity fields (colored shades: positive in red and negative in blue) and potential vorticity (contours: positive in black and negative in green, interval: 2 PVU) **(b)** Same as **(a)** but for theata-e and total precipitation mixing ratio.

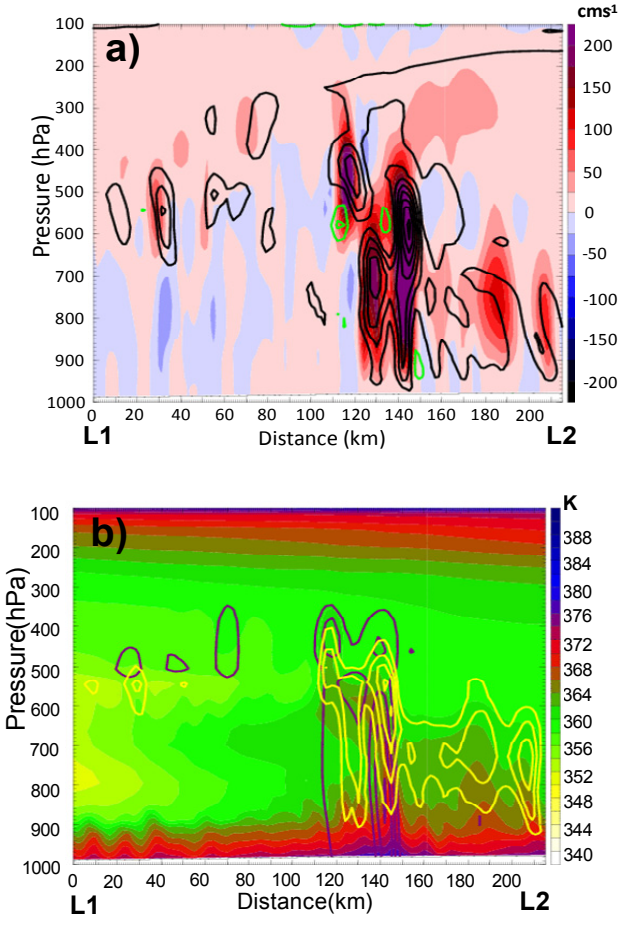

Fig. 12. (a) The cross-section distribution along L1–L2 in Fig. 10b for vertical velocity (shaded) and potential velocity (positive in black and negative in green, interval 2 PVU) at 17:00 UTC 7 August. **(b)** Same as **(a)** but for equivalent potential temperature (shaded), total precipitation mixing ratio (contour in pink) and total cloud mixing ratio (contour in yellow).

convergence zone started to interact with the topography of the southern CMR, and was moving upstream at a speed of about 8 m/s at this line. This propagation was consistent with the typhoon's north-northwestward movement. During these last 5 h, another obvious feature is the downstream wave-like propagations of convective cells inside the convergence zone. There were such signatures in other variables along this cross-section as well (Fig. 10c and d). Additionally, the time evolution along line E1-E2 (Fig. 11) revealed not only the propagations of the wave-train convective cells but also the movement of the typhoon in the vicinity of the convergence zone. On the other hand, the time evolution along line A1-A2 (Fig. 9) depicted mostly the propagation of the wave-train convective cells in the main rainband. Further investigations are warranted to clearly identify the mechanisms between the wave-train convective cells and the convergence zone, but that is beyond the scope of the effort reported here.

To further demonstrate the convergence zone at the outer (southern) boundary of the main rainband studied here, the same variables were extracted on another cross-section L1-L2, which is along 120° E between 22° N and 24° N. Plots on this north-south oriented cross-section are displayed in Figures 12a and b. The convergence-based convective elements with both positive W and PV had a width of only 30 km or less and extended to 300 hPa (Fig. 12a), while the associated cloud/rain fields further indicated the different environments separated by the convergence-based convective elements (Fig. 12b). This upright convective group of cells acted as a narrow wall, separating the calmer air outside the rainband from the more active air inside the band. To the south, W, PV, and cloud/rain activities were all weak, and the θ_E field was less active and more stable. On the other hand, for the atmosphere to the north of the convergence zone, all the fields were stronger and more active because they were inside the main rainband. Particularly, the relatively stronger and less stable θ_E field above the ocean surface supported

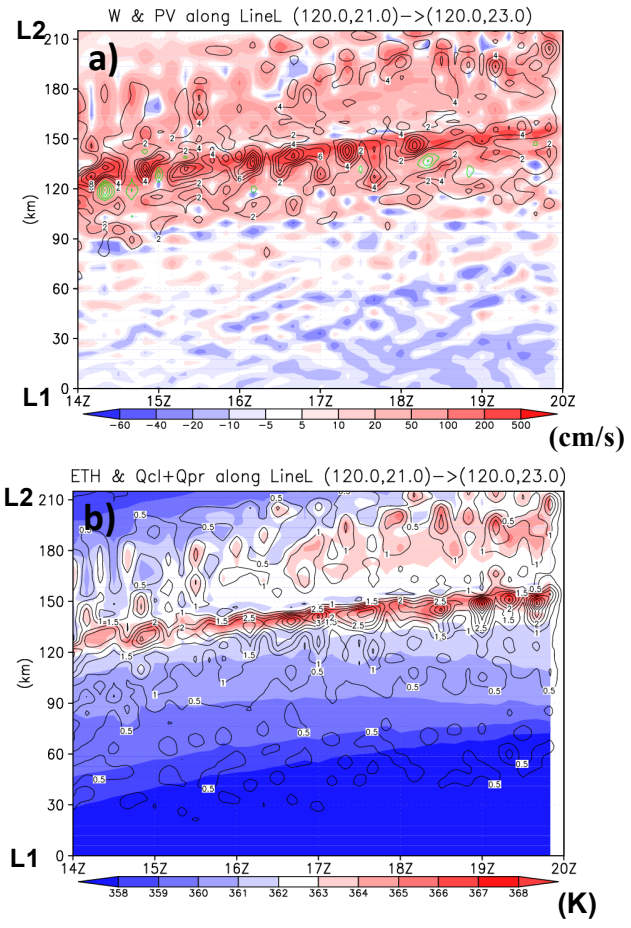

Fig. 13. Simulated results of the temporal variation along cross-section line L1–L2 in Fig. 10b from 14:00 UTC to 20:00 UTC 7 August. **(a)** vertical velocity fields (colored shades: positive in red and negative in blue) and potential vorticity (contours: positive in black and negative in green, interval: 2 PVU) **(b)** same as **(a)** but for theata-e and total precipitation mixing ratio.

the convective activities in this region. Furthermore, there was another weak wave-like signal south of the convective cells supported by the low-level convergence, and centered at an altitude of 550 hPa (Fig. 12). Similar signals were also found south of the convergence zone (Fig. 7). We suggest that internal gravity waves were generated by the typhoon and propagated away from it, as was discussed earlier.

The temporal evolutions of various fields along this cross-section at 750 hPa are summarized in the Hovmoller plots in Fig. 13a and b. The convergence-based convective elements became organized into a band after 14:00 UTC, 7 August, slowly moving northward at a speed of about 1.2 m/s. Of special interest was that the W and θ_E fields evolved from a less organized pattern to a persistent band. Propagating cells of different sizes appeared from time to time, and their spectral characteristics require further analysis.

This fine-resolution numerical simulation has suggested details of dynamical processes that were only partially resolved and revealed by the analysis of the half-degree-resolution analysis data, i.e., the convergence zone. The wave-train rainbands propagated downwind inside the main rainband in the troposphere, and they had their updrafts, positive PV's and convective cells all co-located with the θ_E surges right above the ocean surface. The latent heat flux from the ocean supported the growth of the upward and rotational motions inside the convective cells to enhance the dynamic fields further through latent heat release. As the main rainband gradually moved northward, the downwind moving wave-train convective cells produced further heavy rainfall because of topographical lifting when they reached the western slope of the CMR. Moreover, when the southwest monsoon made its aggressive advance northward with the help of the northerly component of the typhoon circulation, a convergence zone appeared on the southern side of the main rainband. This narrow convergence zone with its vigorous convection contributed to the heavy rainfall at the mountainside as it was lifted. As revealed by the fine-resolution simulation, these two features, the wave-train convection and the convergence-zone convection, were responsible for the heavy rainfall.

From our numerical simulation, the most prominent features are the wave-train convective cells inside the main rainband and the convergence zone at the southern boundary of the rainband. The convergence can be explained by the northerly component of the typhoon's circulation collides with the southerly component of the prevailing southwestern monsoon during the typhoon traversing the Island of Taiwan. This argument can be supported by both coarsely resolved analyzed data and finely resolved simulated data. On the other hand, based on the analyses of the 3-km-resolution numerical simulation, our results seem to have certain characteristics of the vortex Rossby waves (VRWs) found in the simulations of the idealized tropical cyclone (Wang, 2001) and a real hurricane (Chen and Yau, 2001). Also, our estimate of the propagation speed of the wave-train convective cells is consistent with the estimates of vortex Rossby waves of Franklinet al. (2006). However, the wave-train convective cells do not have the appearance of the classical vortex Rossby waves with spiral rainbands connecting to the eyewall. If the VHT wave trains found in our numerical simulation should be the VRWs, they should be the modified VRWs from the classical VRWs under certain processes which need to be explored and identified. It is difficult to argue that those wave-train convective cells inside the main rainband are internal gravity waves, because of the presence of the +PV perturbations co-located with the +W's in the wave-train cells, and the slow propagation speed of those wave trains (Willoughby, 1977; Wang, 2002). Yet other possibilities may exist. One of them is a line or cluster of quasi-stationary or back-building convection generated by the collision of the outflow from storm-generated cold pools and

the prevailing flow at the cold-pool boundary (Doswell et al., 1996; Schumacher and Johnson, 2005; Didlake and Houze, 2009; Houze, 2010). Apparently additional investigations are warranted. Analysis of the radar data of typhoon Morakot and its comparisons with the simulated results, and further numerical experiments and analysis to delineate the dynamic mechanisms will be forthcoming.

5 Summary

In this paper, our primary concerns are the mesoscale processes which caused the heavy rainfall over the southwest region of the island of Taiwan during the passage of typhoon Morakot. First, we observed the larger-scale mechanism of low-level convergence of the northerly component of the typhoon's circulation with the southerly and westerly components of the southwest monsoon, the latter intersecting the Central Mountain Range (CMR). Based on our data analyses, the first stage of the heavy rainfall during 7 and early 8 August was dominated by the N-S convergence south of 23° N in the low troposphere, and the second stage during the rest of 8 August was controlled by the E-W convergence and mountain blocking between 22.5 and 24° N.

From the fine-scale numerical simulation it seems that the heavy rainfall was caused not only by the convergence itself when it interacted with the topography, but also by the wave-train convective cells within the typhoon's main rainband. The convective wave trains were in the form of small rainbands perpendicular to the main one and propagated downwind. As the main rainband moved northward and reached the southern CMR, convective cells inside the narrow convergence zone to the south and those to the north were responsible to heavy rains as they were lifted by the west-facing mountain slopes. The multi-scale nature of tropical cyclones for generating localized heavy rainfall requires further studies utilizing the available observational instruments along with numerical models.

Acknowledgements. We would like to thank the Central Weather Bureau, Taiwan, for providing the data. HH enjoyed the hospitality and support provided by the Research Center for Environmental Changes, Academia Sinica, Taipei, Taiwan. Discussions with Yongsheng Chen, Richard Johnson, Wen-Chau Lee, Chungu Lu, and Yuqing Wang are very much appreciated. We are grateful to the Editor, Timothy J. Dunkerton for his generous effort. This work was supported by NSC96-2111-M-001-004-MY3, NSC 99-2111-M-001-007-MY3 and NSC98-2625-M-492-011.

Edited by: T. J. Dunkerton

References

Brand, S. and Blelloch J. W.: Changes in the characteristics of typhoons crossing the island of Taiwan, Mon. Wea. Rev., 102, 708–713, 1974.

Chane-Ming, F., Roff, G., Robert,L., and Leveau, J.: Gravity wave characteristics over Tromelin Island during the passage of cyclone Hudah, Geophys. Res. Lett., 29(6), 1094, doi:10.1029/2001GL013286, 2002.

Chane-Ming, F., Chen, Z., and Roux, F.: Analysis of gravity-waves produced by intense tropical cyclones, Ann. Geophys., 28, 531–547, 2010, http://www.ann-geophys.net/28/531/2010/.

Chien, F. C., Liu, Y. C., and Lee, C. S.: Heavy rainfall and southwesterly flow after the leaving of typhoon Midulle (2004) from Taiwan, J. Meteorol. Soc. Jpn., 86, 17–41, 2008.

Chen, Y. and Yau, M. K.: Spiral bands in a simulated hurricane, Part I: Vortex Rossby wave verification, J. Atmos. Sci., 58, 2128–2145, 2001.

Chen Y.-L. and Li, J.: Characterisitics of surface air flow and pressure patterns over the island of Taiwan during TAMEX, Mon. Wea. Rev., 123, 695–716,1995.

Chun, H.-Y., Goh, J.-S., and Kim, Y.-H.: Characteristics of inertio-gravity waves revealed in rawinsonde data observed in Korea during 20 August to 5 September 2002, J. Geophys. Res., 112, D16108, doi:10.1029/2006JD008348, 2007.

Dhaka, S. K., Takahashi, M., Shibagaki, Y., Yamanaka, M. D., and Fukao, S.: Gravity wave generation in the lower stratosphere due to passage of the typhoon 9426 (Orchid) observed by the MU radar at Shigaraki (34.85_N, 136.10_E), J. Geophys. Res., 108(D19), 4595, doi:10.1029/2003JD003489, 2003.

Didlake Jr., A. C. and Houze Jr., R. A.: Convective-scale downdrafts in the principal rainband of Hurricane Katrina (2005), Mon. Wea. Rev., 137, 3269–3293, 2009.

Doswell, C. A., III, Brooks, H. E., and Maddox, R. A.: Flash flood forecasting: An ingredients-based methodology, Wea. Forecasting, 11, 560–581, 1996.

Franklin, C. N., Holland, G. J., and May, P. T.: Mechanisms for the generation of mesoscale vorticity features in tropical cyclone rainbands, Mon. Wea. Rev., 134, 2649–2669, 2006.

Ge, X., Li, T., Zhang, S., and Peng, M.: What causes the extremely heavy rainfall in Taiwan during Typhoon Morakot (2009)?, Atmos. Sci. Let., 11, 46–50, 2010.

Hendricks, E. A., Montgomery, M. T., and Davis, C. A.: On the role of "vortical" hot towers in formation of Tropical Cyclone Diana (1984), J. Atmos. Sci., 61, 1209–1232, 2004.

Hong, C. C., Lee, M.-Y., Hsu, H. H., and Kuo, J. L.: Role of submonthly disturbance and 40–50 day ISO on the extreme rainfall event associated with Typhoon Morakot (2009) in Southern Taiwan, Geophy. Res. Lett., 37, doi:10.1029/2010GL042761, 2010.

Houze Jr., R. A.: REVIEW: Clouds in Tropical Cyclones, Mon. Wea. Rev., 138, 293–344, 2010.

Ibrahim, C., Chane-Ming, F., Barthe, C., and Kuleshov, Y.: Diagnosis of tropical cyclone activity through gravity wave energy density in the southwest Indian Ocean, Geophys. Res. Lett., 37, L09807, doi:10.1029/2010GL042938, 2010.

Knutson, T. R., Sirutis, J. J. , Garner, S. T., Held, I., and Tuleya, R. E.: Simulation of the recent multidecadal increase of Atlantic hurricane activity using an 18-km-grid regional model, B. Am. Meteorol. Soc., 88, 1549–156 , 2007.

Kim, S.-Y., Chun, H.-Y., and Baik, J.-J.: A numerical study of gravity waves induced by convection associated with Typhoon Rusa, Geophys. Res. Lett., 32, L24816, doi:10.1029/2005GL024662, 2005.

Kuester, M. A., Alexander, M. J., and Ray, E. A.: A model study of gravity waves over Hurricane Humberto (2001), J. Atmos. Sci., 50, 518–537, 2008.

Lee, C. S., Liu, Y.-C., and Chien, F. C: The secondary low and heavy rainfall associated with Typhoon Mindulle (2004), Won. Wea. Rev., 136, 1260–1283, 2008.

Lin, C.-Y. and Chen, C. S.: A study of orographic effects on mountain-generated precipitation systems under weak synoptic forcing, Meteorol. Atmos. Phys., 81, 1–25, 2002.

Lin, Y.-L., Chiao, S., Wang, T. A., Kaplan, M. L., and Weglarz, R. P.: Some common ingredients for heavy orographic rainfall, Wea. Forecasting, 16, 633–660, 2001.

Lin, Y. L, Ensley, D. B., Chiao, S., and Huang, C. .: Orographic influences on rainfall and track deflection associated with the passage of a tropical cyclone, Mon. Wea. Rev., 130, 2929–2950, 2002.

Montgomery, M. T., Nicholls, M. E., Cram, T. A., and Saunders, A. B.: A vortical hot tower route to tropical cyclogenesis, J. Atmos. Sci., 63, 355–386 , 2006.

Pfister, L., Chan, K. R., Bui, T. P., Bowen, S., Legg, M., Gary, B., Kelly, K., Proffitt, M., and Starr, W.: Gravity waves generated by a tropical cyclone during the STEP tropical field program: A case study, J. Geophys. Res., 98(D5), 8611–8638, 1993.

Qiu, X., Tan, Z.-M., and Xiao, Q.: The Roles of Vortex Rossby Waves in Hurricane Secondary Eyewall Formation, Mon. Wea. Rev., 138, 1092–2109, 2010.

Schumacher, R. S., and R. H. Johnson: Organization and environmental properties of extreme-rain-producing mesoscale convective systems, Mon. Wea. Rev., 133, 961–976, 2005.

Sato, K.: Small-scale wind disturbances observed by the MU radar during the passage of Typhoon Kelly, J. Atmos. Sci., 50, 518–537, 1993.

Skamarock, W. C., Klemp, J. B., Dudhia, J., Gill, D. O., Barker, D. M., Duda, M., Huang, X.-Y., Wang, W., and Powers, J. G.: A Description of the Advanced Research WRF Version 3., NCAR Technical Note, 2008.

Wang, Y.: An explicit simulation of tropical cyclones with a triply nested movable mesh primitive equation model-TCM3, Part I: Model description and control experiment, Mon. Wea. Rev., 129, 1370–1394, 2001.

Wang, Y.: Vortex Rossby waves in a numerically simulated tropical cyclone. Part I: Overall structure, potential vorticity, and kinetic energy budgets, J. Atmos. Sci., 59, 1213–1238, 2002.

Weisman, M. L. and Davis, C. A.: Mechanisms for the generation of mesoscale vortices with quasi-linear convective systems, J. Atmos. Sci., 55, 2603–2622, 1998.

Willoughby, H. E.: Inertia-buoyancy waves in hurricanes, J. Atmos. Sci., 34, 1028–1039, 1977.

Wu, C. C. and Kurhara, Y.: A numerical study of the feedback mechanisms of hurricane-environment interaction on hurricane movement from the potential vorticity perspective, J. Atmos. Sci., 53, 2264–2282, 1996.

Wu, C. C. and Kuo, Y.-H.: Typhoons affecting Taiwan: Current understanding and future challenges, Bull. Amer. Meteor. Soc., 80, 67–80, 1999.

Wu, C. C., Yen, T. H., Kuo, Y. H., and Wang, W.: Rainfall simulation Associated with Typhoon Herb(1996) near Taiwan, Part I: The topographic effect, Wea. Forecasting, 17, 1001–1015, 2002.

Yang, M. J., Zhang, D. L., and Huang, H. L. : A modeling study of Typhoon Nari (2001) at landfall Part I: Topographic effects, J. Atmos. Sci.., 65, 3095–3115, 2008.